High Energy Density Physics 35 (2020) 100731

Contents lists available at ScienceDirect

High Energy Density Physics

journal homepage: www.elsevier.com/locate/hedp

Platform development for *dE/dx* measurements on short-pulse laser facilities

A.B. Zylstra[*,a], J.R. Rygg[b], G.W. Collins[b], C.K. Li[c], J.A. Frenje[c], R.D. Petrasso[c], S.R. Nagel[a], P. Fitzsimmons[d], H. Reynolds[d]

[a] Lawrence Livermore National Laboratory, Livermore, CA 94550, United States
[b] Laboratory for Laser Energetics, University of Rochester, Rochester, NY 14623, United States
[c] Plasma Science and Fusion Center, Massachusetts Institute of Technology, Cambridge, MA 02139, United States
[d] General Atomics, San Diego, CA 92121, United States

ARTICLE INFO

Keywords:
Charged-particle stopping power
TNSA proton generation
Proton isochoric heating

ABSTRACT

Generating benchmark data on charged-particle stopping power in dense plasma is a challenge, motivating new experimental platforms for facilities such as short-pulse lasers. We report on several experiments that aimed to develop a platform for high-precision stopping power measurements at OMEGA EP, specifically developing target-normal sheath acceleration (TNSA) sources, proton isochoric heating, and radiatively heated foams. Integrated experiments were performed to measure stopping power, but several phenomena have been identified that would need to be mitigated for a stopping-power measurement, including irreproducibility of the TNSA sources, spurious electromagnetic fields around proton-heated targets, and cross-talk between the source and subject targets. This work provides a basis for potential future work towards mitigating these problems and performing stopping-power measurements, and is also valuable data for general understanding of TNSA and proton isochoric heating experiments.

1. Introduction

The rate at which charged particles lose energy moving through matter, or stopping power (*dE/dx*), has been a topic of study for more than a century, starting with cold-matter theories from Bragg [1], Bohr [2], Bethe [3], and Bloch [4]. For cold matter theoretical analysis exists constrained by an extensive experimental database [5]. Stopping power in plasmas is a newer topic of study, particularly for high-energy-density plasma (HEDP) conditions that are a challenge for both theory and experiment. Stopping power under these conditions is important as a fundamental plasma transport property and for applications to α particle self-heating in inertial confinement fusion (ICF) [6,7], where the α range directly impacts the hot-spot energy balance [8] and can affect the boundary for achieving a burning plasma [9]. Charged particle stopping powers are also relevant for alternative fusion concepts including proton fast ignition [10] and heavy-ion fusion [11].

Several theoretical models have been published for HEDP conditions, but experimental data is sparse, and the existing data at HEDP conditions are largely generated at long-pulse laser facilities such as OMEGA [12] using implosions [13–16], or with accelerator ion beams [17]. Short-pulse laser facilities, using the chirped-pulse amplification (CPA) technique [18] to achieve high power and intensity, are an appealing capability for *dE/dx* experiments since they can generate novel beams of particles, unique subject plasmas, and are often co-located with facilities including accelerator beams and X-ray free-electron lasers. CPA lasers operating at a high repetition rate could potentially produce large datasets of transport properties, including stopping power. The particle production is significantly shorter duration than long-pulse sources, by up to two orders of magnitude, which could enable probing HEDP samples on time scales rapid compared to the hydrodynamic disassembly timescale, depending on the proton energies used in the experiment and their time of flight to the subject target; the difference in time of flight between proton energies must be small compared to the samples quiescent period. The experimental design must also ensure that higher-energy protons do not appreciably change the target conditions before lower-energy particles arrive. The challenge is conducting measurements with sufficiently high precision to distinguish *dE/dx* models, which the first attempt at stopping power measurements using short-pulse sources, in a pump-probe setup using two TNSA beams to isochorically heat a sample and then measure the stopping power, was unsuccessful at accomplishing due to a large uncertainty from shot-to-shot variability [19].

In this paper we report work towards developing a platform for such *dE/dx* measurements at short-pulse laser facilities. Specifically, we have

* Corresponding author.
E-mail address: zylstra1@llnl.gov (A.B. Zylstra).

https://doi.org/10.1016/j.hedp.2019.100731
Received 23 August 2019; Received in revised form 16 November 2019; Accepted 17 November 2019
Available online 18 November 2019
1574-1818/

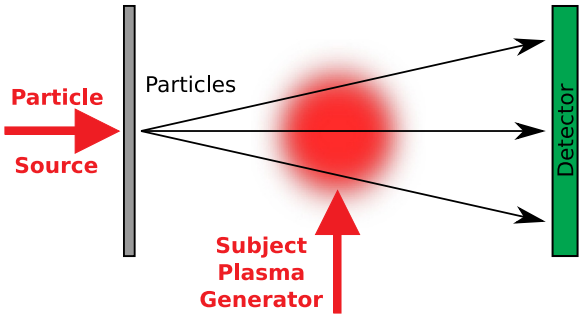

Fig. 1. Top-level schematic for a short-pulse laser experiment to measure *dE/dx*: one beam generates a source of particles, while a second (or several) beam generates a subject plasma. The particles from the source probe the subject plasma and are detected with a spectrometer.

conducted a series of experiments at the OMEGA EP facility [20] on the generation of particle sources, subject plasmas, and the integration of the two. OMEGA EP has two orthogonal CPA beams that can produce up to ~ 1 kJ of energy with 10 ps pulse duration or a few hundred J at best compression (~ 1 ps), with focal spot sizes ~ 20 μm, for intensities up to a few 10^{19} W/cm^2. The source and subject development were untaken with a specific aim of resolving issues relevant to *dE/dx* measurements. Several unexpected effects result in actual measurements of *dE/dx* challenging until they can be mitigated, but are interesting ancillary physics results.

The paper is organized as follows: Section 2 discusses the conceptual design of a *dE/dx* measurement at a short-pulse laser facility, Section 3 describes experiments on particle sources, Section 4 discusses two methods for generating subject plasmas at OMEGA EP, Section 5 discusses several attempts at conducting integrated experiments, and lastly Section 6 concludes the paper.

2. Conceptual design

The top-level concept for performing stopping-power measurements at a short-pulse laser facility is shown in Fig. 1. A short-pulse beam is used to generate a source of particles, which probe a subject plasma that is generated by a second short pulse, or by one or more long-pulse beams. The downshifted particles, after transit from the source through the subject plasma, are then measured on a detector.

2.1. Particle sources

The Target-Normal Sheath Acceleration (TNSA) [21] mechanism is a well-known technique for producing high fluences of energetic ions, mainly in a forward-directed beam, and is the mechanism used in this work to generate the particle source. These ion beams have many potential applications including proton radiography [22,23], proton probing, and proton isochoric heating [24]. Typically mid- or high-Z flat foils are used as source targets for these experiments. In this work, several advanced target types were tested on the OMEGA EP laser [20]. In Section 3.1, several types of substrate material were used to study the material's effect on proton beam uniformity, which is also critical for proton radiography applications. In Section 3.2, microstructured plastic-coated targets were used in a replication experiment of previously-published results showing quasi-monoenergetic peaks in the TNSA spectrum [25]. For an accurate stopping-power measurement the particle source would either need to be sufficiently repeatable shot-to-shot that variability does not limit the measurement precision, or the experimental setup would need to include a second diagnostic measuring the source spectrum. In theory the measurement of a well-characterized broadband particle source, downshifted through a subject target, measures the stopping-power relationship versus energy as the downshifted spectrum is a unique convolution of the incident spectrum

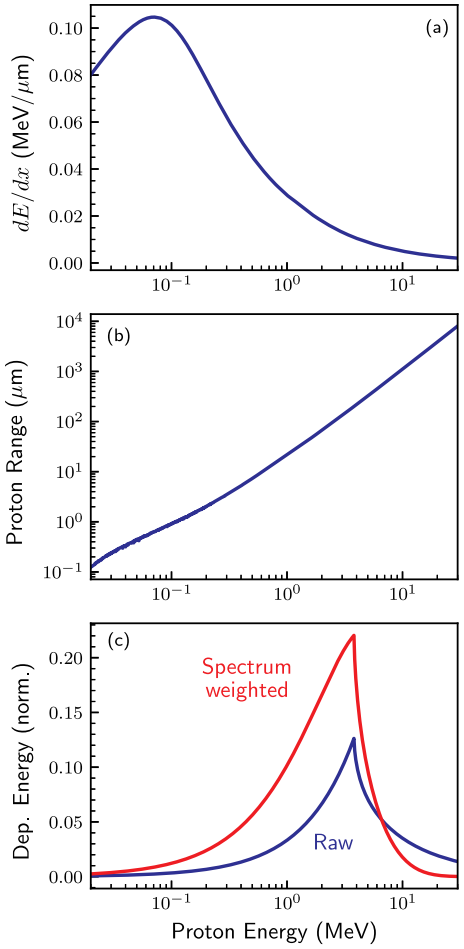

Fig. 2. Stopping-power calculation for proton isochoric heating of plastic, including the cold-matter *dE/dx* calculated using SRIM [5] (a), the range of protons in plastic (b), and the deposited energy versus proton energy for a 200 μm thick sample (c), area normalized.

and the stopping power. However, the ability to infer the stopping power will be limited by experimental measurement uncertainties and second-order effects including straggling, which causes a statistical energy broadening as the particles slow down, and scattering, which causes angular deflection.

It is simpler and potentially more precise to use a quasi-monoenergetic source to measure the stopping power at a particular energy on each shot. One route to this is advanced TNSA targets, as mentioned above; another promising technique that could be applied to these measurements is to use spectral filtering of the broadband energy distribution, which has recently been developed for TNSA proton beams [26,27].

2.2. Subject plasmas

Proton isochoric heating using petawatt lasers [24] is potentially an interesting technique for stopping power experiments, which require a 'subject' plasma be generated in an interesting state to probe. Fast proton beams generated by the TNSA mechanism can be used to rapidly and quasi-volumetrically heat a sample of solid-density material to Warm Dense Matter (WDM) conditions. Fig. 2 shows the cold-matter stopping power, range, and deposited energy for protons in a 200 μm thick sample of plastic. In Fig. 2c the 'raw' deposited energy corresponds to the energy depositions for protons of specific energies, with a peak corresponding to a proton where the range is matched to the sample thickness. The spectrum weighted curve includes a weighting

function representative of a typical TNSA spectrum ($\propto \exp[-E_p/5]$ with E_p in MeV). Protons of a few MeV effectively heat the sample approximately isochorically to temperatures of $\sim$ eV to $\sim$ 10 s of eV while remaining at solid density. At these conditions an accurate measurement of the stopping power also requires reasonably accurate knowledge of the target ionization state (see Ref. [13] and [19]).

At these conditions the hydrodynamic disassembly time is approximately half the target thickness divided by the sound speed, $d/2c_s$, where $c_s = \sqrt{\gamma \bar{Z} k_B T_e / m_i}$ with γ as the adiabatic index, $\bar{Z}$ and m_i the ionization state and ion mass, and $k_B T_e$ the temperature. For a plastic target $c_s \sim 5\sqrt{\bar{Z}T_e}$ μm/ns where T_e is in eV. In the WDM regime where $\bar{Z} \sim 1.5$, then $c_s \sim 20$ μm/ns at 10 eV and the target disassembly time is several ns.

It is also interesting to generate lower-density but higher-temperature plasmas. One route to doing this using a small number of long-pulse beams, which are available at facilities like OMEGA EP, to heat a high-Z halfraum that generates X-ray radiation incident upon a low-density foam. This concept has been proposed for novel ion stopping measurements on several-beam laser facilities [28–31]. This is shown schematically in Fig. 3. The X-ray drive launches a Marshak wave into the foam, maintaining the initial density. Simulations using HYADES [32] are shown in Fig. 4 for a 150 eV temperature in the hohlraum driving a 50 mg/cc foam. This generates a plasma at $\sim$ 110 eV and the initial foam density $\sim$ 50 mg/cc. With a width of $\sim$ 600 μm and a sound speed $c_s \sim$ 90 μm/ns the hydrodynamic disassembly time is $\sim$ 3 ns.

2.3. dE/dx measurements

The integrated dE/dx measurement is to combine the source and subject components in a single shot and measure spectra to sufficient accuracy to discriminate stopping-power models at interesting and relevant conditions. Some example stopping-power calculations are shown in Fig. 5(a) and (b) show conditions relevant for proton isochoric heating (solid density plastic at 10 eV), while (c) and (d) show conditions appropriate for halfraum-heated foam experiments (50 mg/cc CH at 110 eV). Plasma calculations using the Li-Petrasso (LP) [33–35], Brown-Preston-Singleton [36], and Maynard-Deutsch [37,38] are shown and compared to the cold-matter stopping power from SRIM [5]. Since the plasmas are partially ionized the total stopping power is calculated using an estimated ionization state with separate prescriptions for bound and free electrons (see Ref. [13]). For proton energies of a few MeV, the plasma theories differ from cold-matter stopping by 10–20%. For distinguishing the plasma stopping theories, the halfraum-heated foam plasma probed by protons of $\sim$ 1 MeV is most promising; this is a sensitive measurement since the protons are nearing the Bragg peak in the stopping power. The requirement for proton spectral precision is thus better than 10% to differentiate the plasma stopping from cold, and better, ideally a couple of percent, for differentiating between different plasma stopping models.

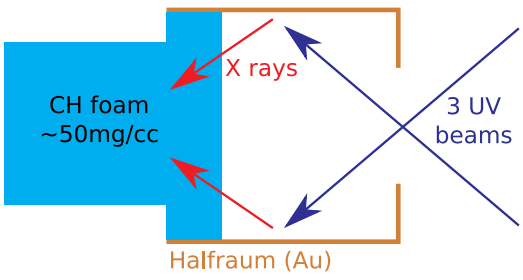

Fig. 3. Concept for heating a foam sample using UV long-pulse beams to generate thermal radiation in a halfram.

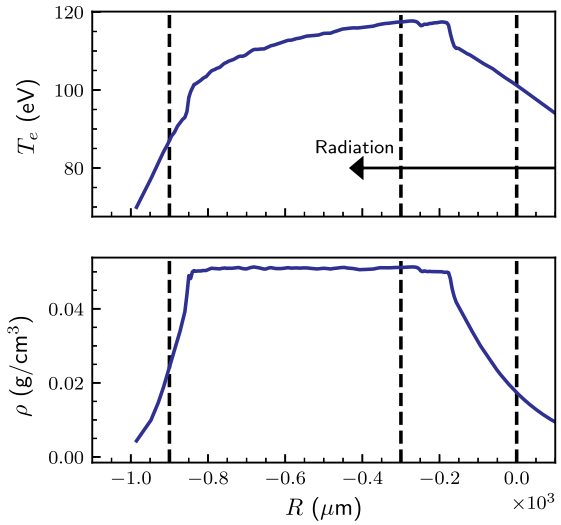

Fig. 4. Simulation of the halfraum-heated foam concept (Fig. 3), showing electron temperature (top) and mass density (bottom). The 50 mg/cc CH foam is recessed 300 μm into the halfram, so the probing region would be between 300 and 900 μm. The orientation has the foam extending to $-r$ values, with the radiation flowing from right to left. The plasma conditions are plotted 2 ns after the start of the hohlraum drive.

3. Source development

As described in the previous section, the goal of this platform is to use TNSA targets as the particle sources. Building on previous experience at the OMEGA EP facility, several experiments were conducted to attempt improvements to the source characteristics using advanced types foil targets.

The geometry for TNSA proton source experiments is shown schematically in Fig. 6. The target is a planar source foil with the short-pulse beam incident upon the front surface. The primary diagnostics are radiochromic film (RCF) [39] and a Thomson-Parabola Ion Energy analyzer (TPIE) [40–42]. To support several experiments, including this work, a smaller-field 1.6 kG permanent dipole magnet was purchased for the TPIE system [40]. The calibration of this magnet is described in Ref. [43].

3.1. Proton source foils

Non-uniform proton emission from TNSA foils is commonly observed at OMEGA EP, where 10 μm-thick Au foils are typically used [23]. The surface quality of these targets can be poor, with thickness variation up to 10% expected. Since the TNSA mechanism is highly sensitive to the conditions on both target surfaces, it has been expected that these targets may have degraded uniformity due to the poor surface quality. Previous experiments on the TITAN laser facility found improved uniformity with improved target surface quality [44], motivating similar experiments at OMEGA EP.

Four different types of planar foils were made and tested. The foils types and their RMS surface roughness are summarized in Table 1. First, 10 μm thick Au foils were purchased from Goodfellow. Thicker Au substrates were machined at General Atomics (GA) to the same 10 μm thickness but substantially improved surface quality. Wafers of silicon (Si) and chemical vapor deposition (CVD) diamond were coated with 1 μm of Au on each surface. The advanced targets have a $10-100\times$ improvement in surface roughness compared to the standard Goodfellow foils.

The foils were all driven by one short-pulse beam of OMEGA EP using 'best compression' (1 ps pulse). The uniformity is diagnosed with RCF. Three shots with identical high-intensity drive and various foil types are shown in Fig. 7. The wafer foils, with much less surface

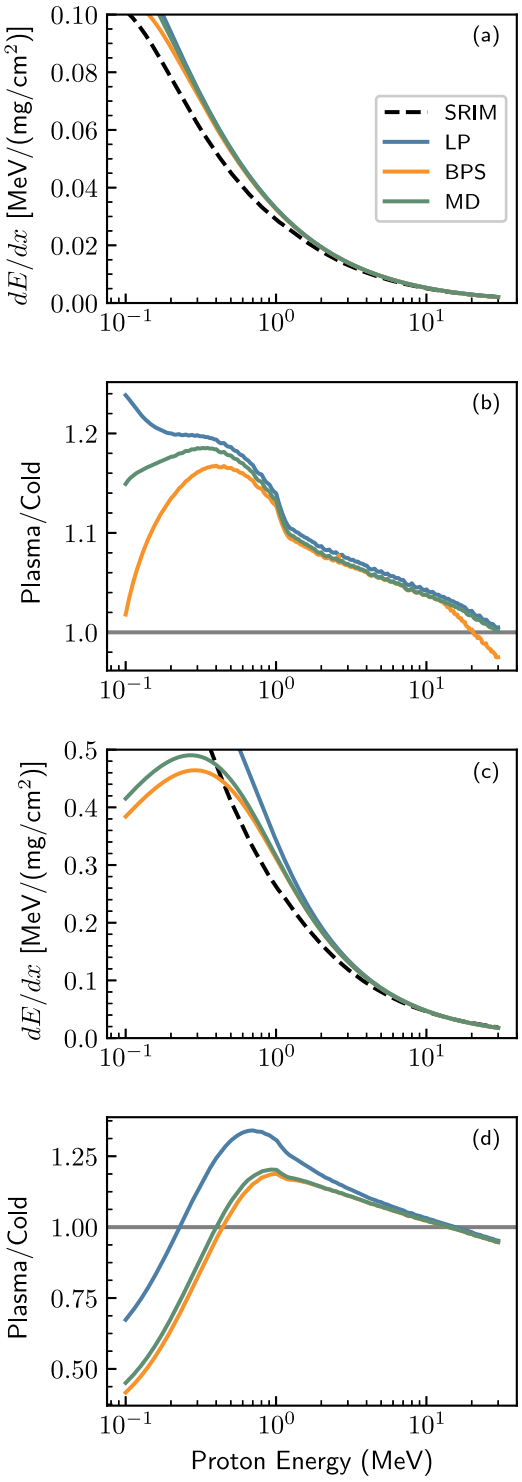

Fig. 5. Stopping power (a, c) and difference between plasma and cold matter (b,d) for example subject plasmas relevant to proton isochoric heating (a,b) and halfraum-heated foams (c,d). The proton isochoric heating target is assumed to be CH with T_e = 10 eV and $n_i = 10^{23}$ cm^{-3}, while for the halfraum-heated foam we take T_e = 110 eV and $n_i = 5 \times 10^{21}$ cm^{-3}.

roughness, still exhibit significant spatial (transverse) non-uniformities in the emitted proton beam. Similarly, a comparison of Goodfellow and GA-machined Au foils is shown in Fig. 8.

The images clearly show that the foils with very poor surface uniformity (the Goodfellow Au) have significant high-mode quasi-filamentary structures in the emitted proton beam, which are not observed

Table 1
Types of target foils used, and their RMS surface roughness (δT).

Foil type and thickness	RMS δT (nm)
Goodfellow 10 μm Au	800–900
GA-machined 10 μm Au	30
50 μm Si Wafer with 1 μm Au coating	4
50 μm CVD Wafer with 1 μm Au coating	≤ 10

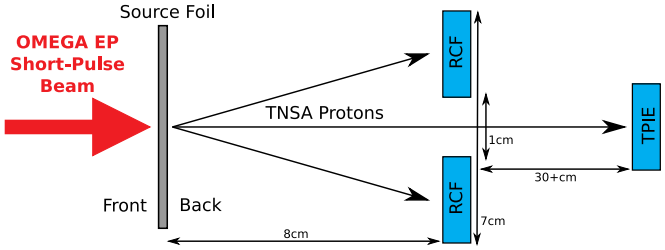

Fig. 6. Experimental geometry for the TNSA proton source experiments. The short-pulse laser is incident upon the front surface of a source foil. Ions accelerated from the rear surface are detected by RCF and the TPIE spectrometer through a 1cm hole in the RCF film pack.

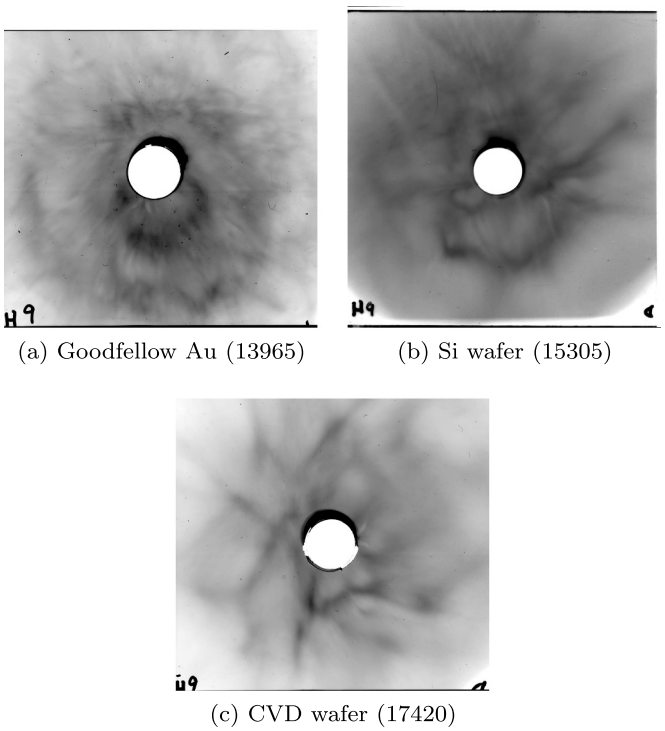

(a) Goodfellow Au (13965) (b) Si wafer (15305)

(c) CVD wafer (17420)

Fig. 7. Proton beam images using 400 J/1 ps drive (~ 3 × 10^{19} W/cm^2) with three target types. RCF filtering corresponds to a peak sensitivity to 35 MeV protons. All target types display significant transverse non-uniformities. Shot numbers are given for each experiment in parentheses. The hole in the middle of the film is for the TPIE spectrometer LOS (see Fig. 12). Each film is 7cm square (see Fig. 6).

in the beams from smoother foils. However, the advanced foils have very significant lower-mode structure in the emitted beams, which would be extremely problematic for radiography applications.

One common factor is the laser spot uniformity on a foil, which is shown in Fig. 9. The non-uniform laser illumination is typical for experiments at EP, and may seed instabilities. In particular, prior experiments and simulation work have shown that resistive filamentation instabilities can develop as the laser-accelerated electrons propagate through the solid source target [45,46]. The non-uniform laser

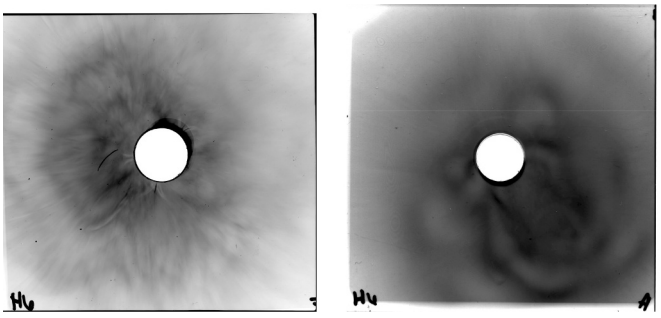

(a) Goodfellow Au (13971) (b) GA Au (15296)

Fig. 8. Proton beams produced by using 200 J/1 ps ($\sim 1.5 \times 10^{19}$ W/cm^2) laser pulses incident upon the two types of Au target. RCF filtering corresponds to a peak sensitivity to 18 MeV protons (lower than Fig. 7 due to the lower drive energy). Both target types display significant transverse non-uniformities.

irradiation may seed an initial non-uniformity in electron flux, which will accentuate through the filamentation instability. The prior literature predicts a stabilization of the resistive filamentation instability in diamond wafer targets at lower intensity due to the low-temperature resistivity behavior of diamond [45].

To test this, the same targets were shot with a factor of 10 × less energy (40 J/1 ps). The results are shown in Fig. 10. While non-uniformities are still apparent in all experiments, the CVD wafer qualitatively appears to have the best uniformity, which may support prior results, and the hypothesis that the focal spot non-uniformity is causing the observed variation at higher intensity. However the degree of non-uniformity is still concerning for a stopping-power measurement as the spectrum may change spatially, which motivates additional changes such as significantly thicker foils (see Section 5.2).

3.2. CH-coated foils

Shots with CH-coated foils were also conducted. The motivation for these experiments was to reproduce experiments reported by Schwoerer et al. [25], which showed quasi-monoenergetic peak structures in the spectra of TNSA protons when using microstructured foils. A large dot (500 μm square) of CH was deposited onto the rear surface of a TNSA planar foil. The size of the coating is much larger than the laser spot size (~ 20 μm). The data taken at EP using microstructured targets is shown in Fig. 11.

When driven at high intensity, one shot of data (13963) does display a clear peak at $E_p \sim 2.5$ MeV, similar to the Schwoerer results

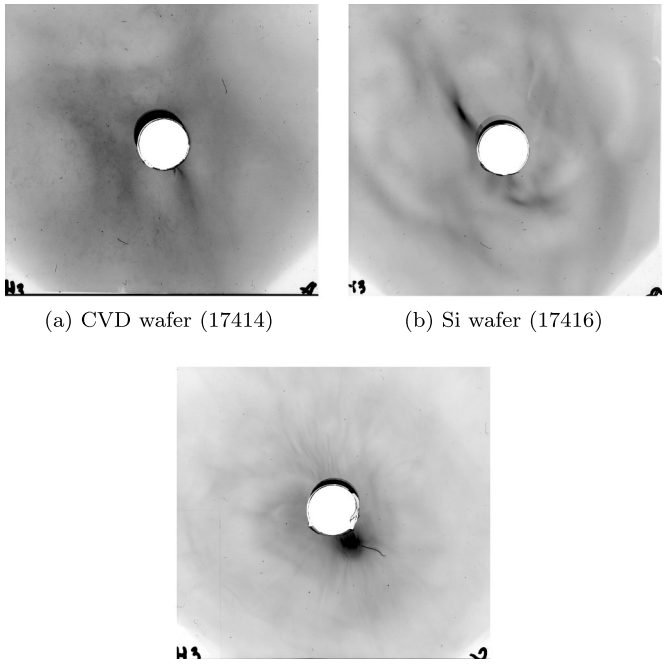

(a) CVD wafer (17414) (b) Si wafer (17416)

(c) Goodfellow Au (17418)

Fig. 10. Images of proton beams using 40 J/1 ps ($\sim 3 \times 10^{18}$ W/cm^2) laser pulses incident upon three target types. RCF filtering corresponds to a peak sensitivity to 9 MeV protons.

(Ref. [25]). However, attempts to repeat the experiment (shots 13973, 15301) result in very different proton spectra. The sharp cutoffs ~ 1 MeV in these spectra are not typical of TNSA. We hypothesize that the cutoff results from transverse non-uniformities in the proton emission.

At low intensity (17414), a similar result is seen, with a peak at ~ 1 MeV. In this case we have a direct comparison to an identical shot without plastic coating (17424). However the repeatability or reliability of this peak generation has not yet been tested.

We conclude that the production of a quasi-monoenergetic peak in the proton spectrum from such microstructured papers, as claimed in Ref. [25], is possible on OMEGA EP but highly irreproducible, and therefore not suitable for *dE/dx* experiments without improved reproducibility.

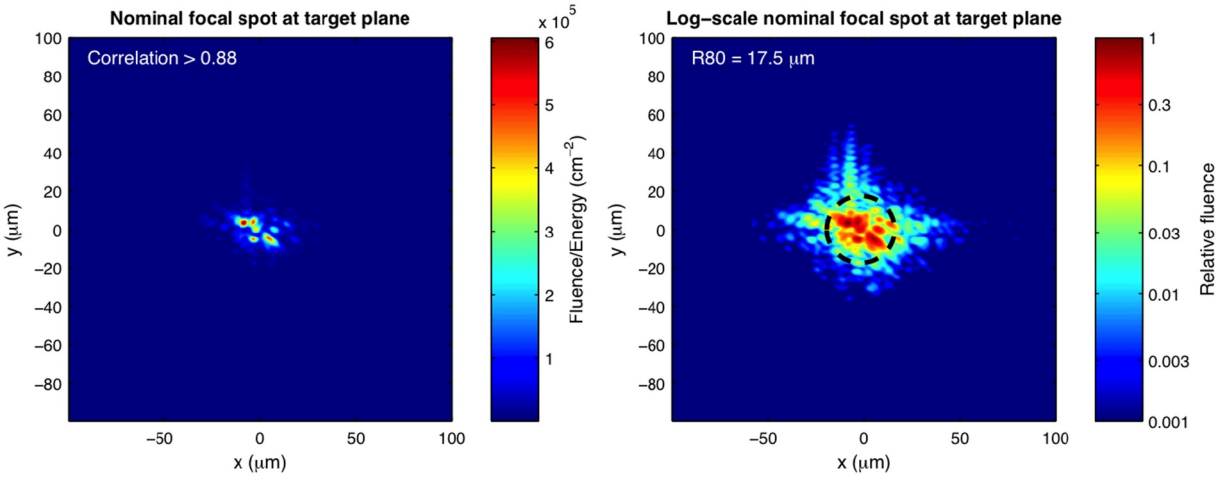

Fig. 9. Laser focal spot shape for shot 15301. Significant non-uniformity in the laser illumination on the foil is routinely seen at EP.

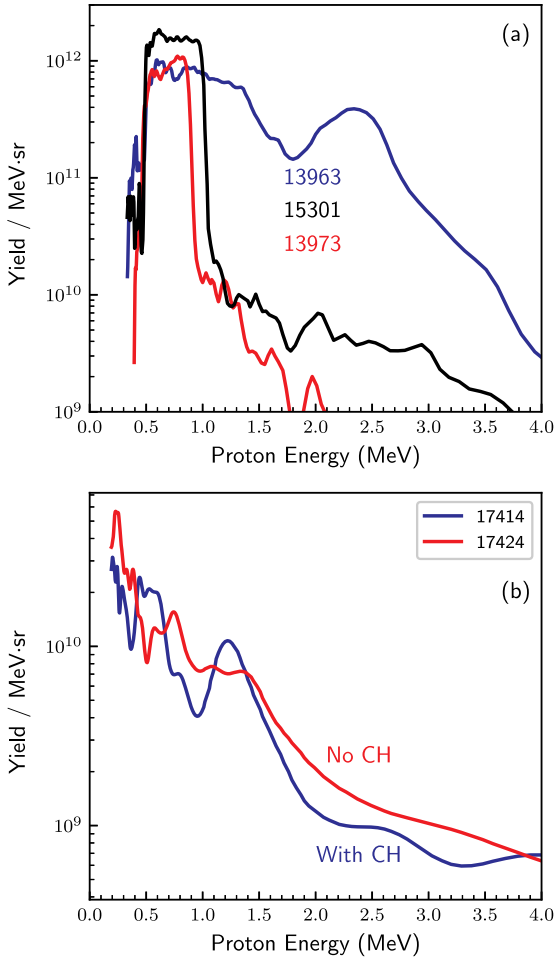

Fig. 11. Proton spectra measured with TPIE. These protons were produced using high-intensity drive (400 J/1 ps, $\sim 3 \times 10^{19}$ W/cm^2, a) or low-intensity drive (40 J/1 ps, $\sim 3 \times 10^{18}$ W/cm^2, b) onto microstructured foils. The high-intensity data (a) all have the CH coating, while at low intensity (b) we have a comparison with and without CH.

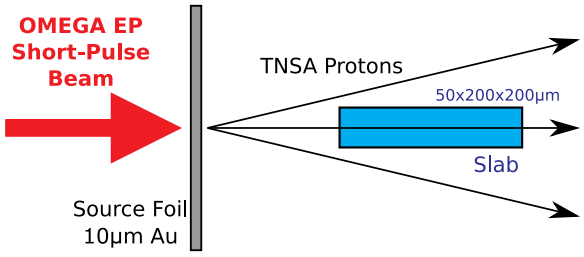

Fig. 12. Experimental configuration for studying proton isochoric heating. Protons generated by TNSA traverse and heat a plastic (CH) slab (blue). Broadband area-backlit X-ray radiography (not shown) is conducted perpendicular to the page. (For interpretation of the references to color in this figure legend, the reader is referred to the web version of this article.)

4. Subject development

4.1. Proton isochoric heating

In this work, experiments were conducted at EP using TNSA-generated protons to heat a sample (see Section 2.2), which is diagnosed with self-radiography and orthogonal X-ray radiography.

The experimental configuration is shown in Fig. 12. One of the EP short-pulse laser beams was incident upon a planar foil, which was typically a 10 μm-thick Au foil. The generated protons traverse a slab of plastic (dimensions 200 × 200 × 50 μm), heating the slab by energy deposition. The stopping power of protons in the slab is shown in Fig. 2.

The slab is 200 μm thick along the proton's path, corresponding to the total range of a 3.8 MeV proton, which is apparent as the peak in the energy deposition profile in Fig. 2. Most of the proton heating comes from particles around this energy. When the exponentially-decaying spectrum for a TNSA source is taken into account, more of the heating comes from lower-energy protons. Since the low-energy particles will be ranged out in the slab, this may cause longitudinally non-uniform heating.

4.1.1. X-ray radiography to characterize slab heating

X-ray radiography was used to characterize the expansion of the plasma slab after proton heating. The radiography is perpendicular to the proton heating beam, and views the slab 'edge-on', as it appears in Fig. 12. A depleted-uranium foil is driven by two long-pulse OMEGA EP beams (#3 and #4) with a 2 ns square pulse, up to 2 kJ/beam, and with SG8 DPP. The resulting X-ray emission area is large enough for area backlighting. A 3 μm-thick Al foil is placed between the backlighter foil and the proton heating target to reduce X-ray preheat.

A standard X-Ray Framing Camera (XRFC) was used to record the radiographs. The XRFC was configured with 4 strips and a 12-pinhole array. The soft X-ray snout (SXS) was used, which consists of a straight-through central channel and two mirror-reflected channels on each strip. The mirror channels are only sensitive to soft X rays, thus reducing hard-photon background in the images. Al filtering was used to optimize the signal strength, and the strips were timed with 500 ps between them, starting 400 ps before the heating, and with a 200 ps pulse-forming module (PFM). The data are recorded on Biomax film.

The data from shot 15308 is shown in Fig. 13. On this shot, the proton heating drive was 500 J/10 ps ($\sim 4 \times 10^{18}$ W/cm^2). The slab is roughly centered in each image. The feature extending up and to the right (left) is the stalk in the central (mirrored) channels. The proton heating beam goes left-to-right (right-to-left) in the central (mirrored) images. The first strip is taken before the heating, with subsequent strip delays of 0.1, 0.6, and 1.1 ns relative to the proton heating.

The slab is expanding in strips 2 through 4, with the expansion most obvious in the 4th strip (bottom of the image). The tip of the slab is also observed to expand farther in a 'mushroom' shape, which suggests longitudinally non-uniform heating along the proton beam direction.

The radiography data are first converted into X-ray flux using the step wedge calibration. Each frame is background-subtracted using regions between the frames. Within a given frame, a 2-D polynomial fit to the backlighter profile is subtracted from the image to obtain the target opacity image. Supergaussian fits across the slab at two locations are used to correct for the image's rotation. The image is also converted to image-plane-distance units using the known magnification. The final result of this analysis for an example from (strip 1, 3rd frame) is shown in Fig. 14.

Profiles of the slab absorption from this image analysis are used to infer the heating dynamics. For example, profiles at various depths from 10 to 90 μm into the slab, along the proton propagation direction, are shown in Fig. 15. The profile near to the tip of the slab (10 μm) is clearly different from the more recessed lineouts.

A straightforward analysis technique is to fit the data and infer the increase in FWHM due to the slab expansion, which can be directly compared to simulations. The images from frame 3 of each strip are analyzed at a depth of 30 μm into the slab. The profile is fit with a supergaussian:

$$f(y) = A \times \left(\frac{1}{2^{1+1/N}\sigma} \frac{1}{2\Gamma(1+1/N)} \right) \exp\left[\frac{(y-\mu)^n}{2\sigma^N} \right] + B, \quad (1)$$

where y is the coordinate perpendicular to the proton direction. The fit parameters are the amplitude A, an offset B, the supergaussian width σ, mean position μ, and order N. Fits to three profiles are shown in Fig. 16.

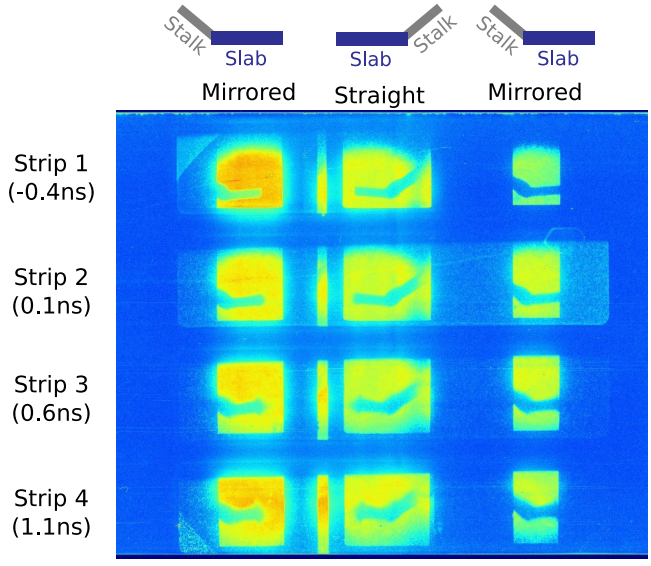

Fig. 13. The raw XRFC data from shot 15308. The x rays image the slab and part of its stalk. The protons are incident upon the tip of the slab opposite the stalk. With the snout used, the center channel is straight through while the two side channels are mirror images. The color scale denotes signal levels on the camera.

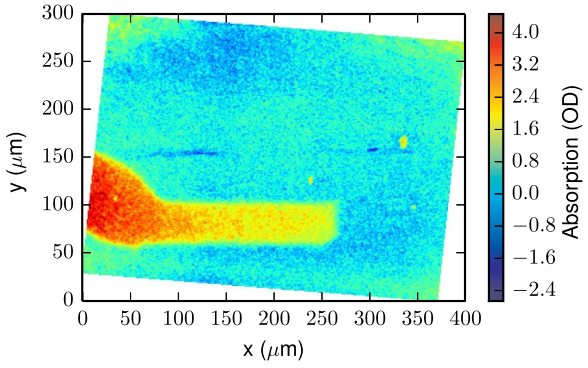

Fig. 14. Reduced third image of first strip (Fig. 13), showing the stalk entering from left and the slab. The protons are incident upon the slab opposite the stalk (at right of the image).

The FWHM from the fits in Fig. 16 is used to compare to simulations in Fig. 17. The expansion into vacuum of a CH slab artificially pre-heated[1] to various temperatures was modeled with the HYADES radiation-hydrodynamics code [32]. The simulated density (OD) profile is motion- and resolution-blurred to calculate an inferred simulation FWHM of the profile.

The time axis is normalized so that the proton heating occurs at $t = 0$. One radiograph was taken before the heating occurs, resulting in a FWHM = 50 μm, the initial slab width, as expected. After the heating, the slab is observed to rapidly puff up to a 75 μm thickness in $\sim$ 0.3 ns, and then to 80 μm thickness in 0.8 ns.

This behavior clearly contradicts the hydrodynamic result, as illustrated by the curves. In the simulation, FWHM initially decreases as the rarefaction wave propagates into the solid slab. After the two-sided rarefaction meets in the middle, the material is all expanding and the calculated FWHM increases rapidly.

The temporal history of the slab expansion is not driven by

[1] Since the proton heating occurs rapidly ($\sim$ ps) compared to dynamical timescales ($\sim$ 100 s of ps), the HYADES simulations are configured using an initial temperature to approximate the heating process.

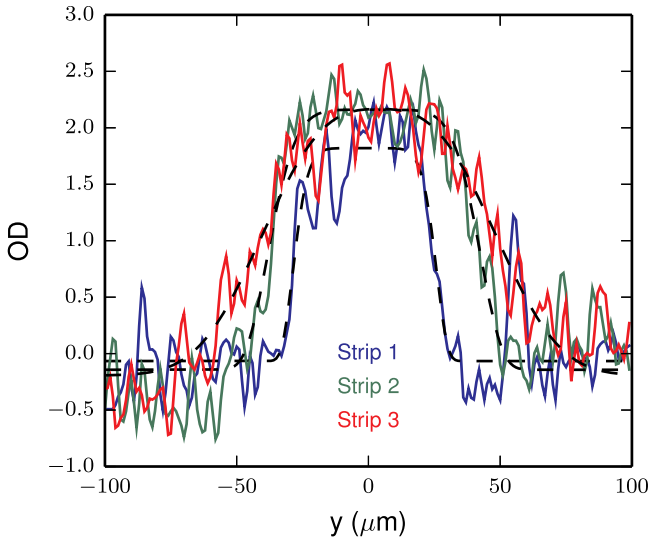

Fig. 16. Supergaussian fits to optical density profiles at a depth of 30 μm, obtained from frame 3 images using strips 1, 2, and 3.

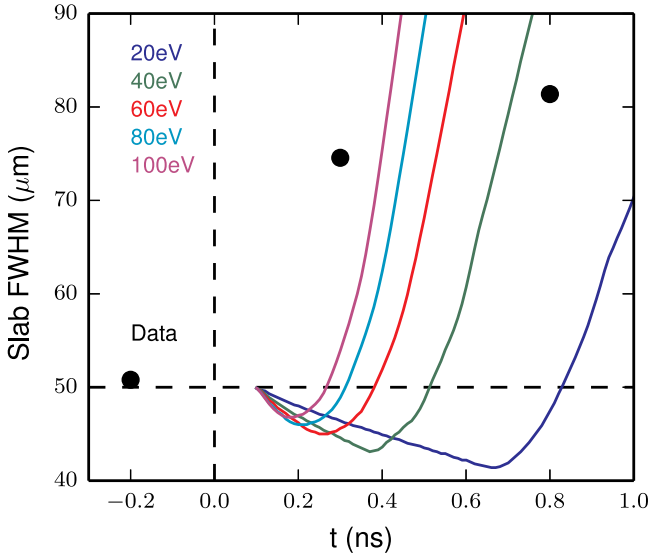

Fig. 17. Comparison of experimental and simulated FWHM vs time for the slab expansion. Simulated curves are shown for various initial temperatures.

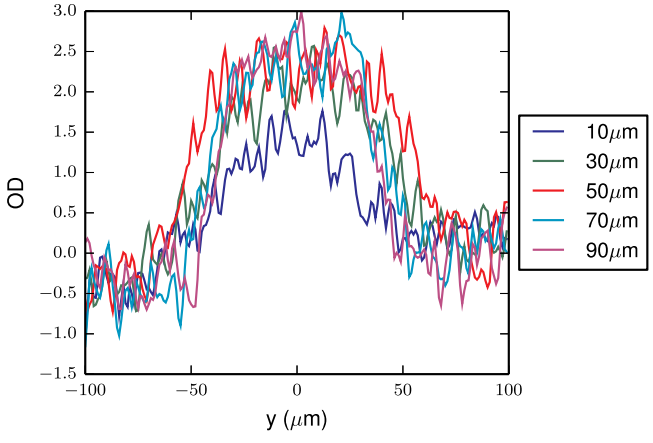

Fig. 15. Optical density of the slab at several depths (corresponding to distance along the proton heating path), a measure of the heating uniformity along the proton beam.

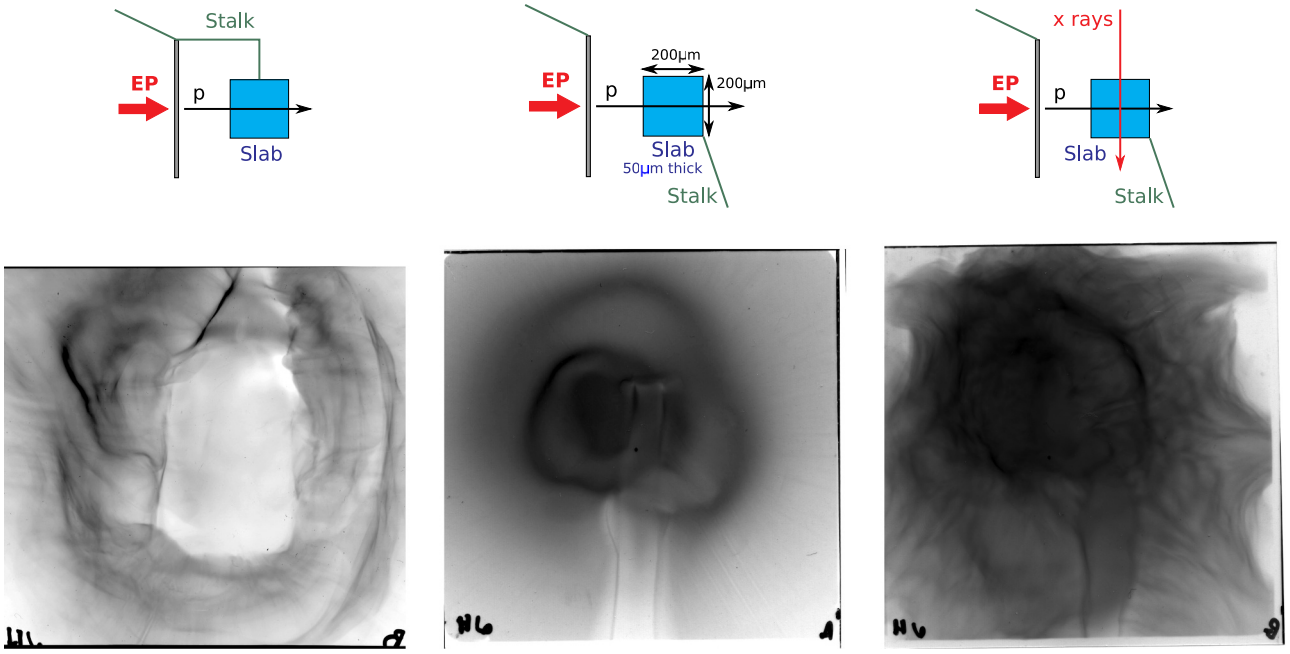

(a) 13964 (b) 15310 (c) 15306

Fig. 18. Self-radiography of proton heating slab target. The proton heating beam, after passing through the slab, is recorded on RCF. These films correspond to 18 MeV protons. The short-pulse drive is 500 J/10 ps ($\sim 4 \times 10^{18}$ W/cm^2) in all cases. For shot 13964 (left), the slab was attached to the proton source target via stalk. For shot 15310, the slab was independently positioned. Shot 15306 is like 15310, but with the X-ray backlighter turned on 500 ps before the proton heating occurs. Cartoons above each RCF image depict the geometry. The image magnification is 80 × ; a 200 μm scale bar is shown in the center. In this view, the slab is initially 200 μm vertical by 50 μm horizontal.

hydrodynamic rarefaction. Another possibility is that the slab motion is driven by the Lorentz force. The petawatt laser interaction generates an extreme flux of energetic electrons, which pass through the slab, followed by the ion beam. This has the potential to induce electromagnetic fields in and around the slab target. Evidence for this is explored in Section 4.1.2. If the slab is charged (either positively or negatively) by the TNSA particle flux, then electrostatic self-repulsion will lead to a rapid expansion in a 'Coulomb explosion'. Neutralization of the charge will occur over several hundred ps via a stalk return current [47,48], which could explain the rapid expansion and subsequent apparent deceleration observed. Unfortunately, this effect means that inferring a temperature from the slab expansion is not possible.

4.1.2. *Electromagnetic fields around the slab*

In these experiments, the proton beam is recorded on RCF after passing through the slab target. This data is useful to diagnose potential electromagnetic fields that might develop around the slab. Three radiographs from the experiments are shown in Fig. 18. All experiments used identical laser conditions (500 J/10 ps short-pulse drive) and targets (10 μm Au source foils, 200 × 200 × 50 μm CH slabs). The difference between 13964 (left) and 15310 (center) is how the slab is attached: via stalk to the source foil (13964) or by an independent stalk (15310). The difference between 15310 and 15306 is that the orthogonal X-ray backlighter was turned on for 15306.

Shot has an obvious qualitative difference in the image than the other two, in that the slab is substantially magnified relative to the expected geometric magnification. This indicates an electric or magnetic field:

$$\theta_B = \frac{q}{\sqrt{2m_p E_p}} \int B_\perp d\ell, \qquad \theta_E = \frac{q}{2E_p} \int E_\perp d\ell. \tag{2}$$

The deflection (θ) depends on the path-integrated perpendicular electric or magnetic field, and the proton energy (E_p). Typically E and B would be discriminated by using multiple proton energies. Unfortunately in this experiment, the other film images are low quality. It is clear, however, that the slab image is uniformly magnified, which is highly suggestive of an electric field.

In this image, the maximum deflection is $\theta_E \sim 17^\circ$ for $E_p = 18$ MeV. This corresponds to a value of $\int E_\perp d\ell \sim 10^7$ V. For a scale length of hundreds of μm, that is an electric field of tens of GV/m. If the drop to zero potential occurs over mm scale, then the slab charging is of order tens of MV, which is comparable to the petawatt-induced charging of the foil target, which accelerates the TNSA ions. Since the slab is small and mounted close to the foil (1mm away) compared to the foil lateral dimensions (2mm), the entire target must charge and discharge. Unfortunately this significantly complicates the proton heating dynamics. The lack of significant charging effects[2] in shot 15310 clearly suggests that an independent stalk mount is desirable for proton isochoric heating experiments.

The other clear observation is that the presence of the X-ray backlighter induces significant chaotic structure in the self-radiograph (shot 15306). Since the drive beams for the backlighter are turned on 500 ps before the proton heating occurs, the X-ray flux may affect the proton heating targets. The X-ray flux from the backlighter is not sufficiently intense to bulk heat and drive the targets, but could potentially create a small amount of tenuous plasma surrounding the proton source targets. This could have an effect on the TNSA proton generation, or the electromagnetic fields surrounding the two targets, plausibly explaining the observed self-radiograph.

[2] Transverse non-uniformities in the observed radiograph may result from field structures around the slab, but it is also very likely that they result from non-uniformities in the proton beam emission (see Section 3).

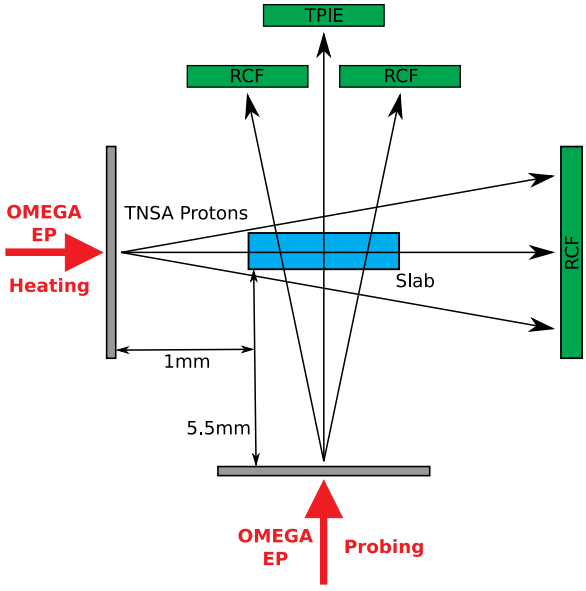

Fig. 19. Experimental geometry with both proton heating (horizontal) and proton probing (vertical). The proton heating beam self-radiograph is recorded on RCF (8cm from TCC). The proton source beam is recorded on RCF (8cm) and the TPIE spectrometer (40+ cm from TCC).

5. Integrated experiments

5.1. Proton isochoric heating

Combining the proton source and proton heating techniques raises the issue of crosstalk between them. Preliminary integrated experiments have been conducted to assess this possibility, where proton heating is used to create a subject plasma, and a proton source (Section 3) is generated after the heating, with the probing protons passing through the subject plasma orthogonal to the original heating protons. This experimental geometry is shown in Fig. 19. The resulting RCF images of the probing proton beam (see Fig. 19) are shown in Fig. 20. Based on the experimental geometry, the projected image of the slab was expected to be centered on the TPIE spectrometer line of sight, which is the white circle in the RCF images. Instead, protons going through the slab are displaced by ~ 1 cm in the image plane. In the experiment, no target or diagnostic misalignment can explain this much offset. In addition, the offset is repeatable, and observed on both shots with and without proton heating (top and bottom of Fig. 20).

The deflection angle of the protons is inferred from the slab's centroid location as a function of proton energy, and plotted in Fig. 21. The deflection angle is found to be $\sim 8-9$ degrees for a wide range of proton energies (15–35 MeV). This is inconsistent with a constant electric or magnetic field deflection (see Eq. (2)) - the expected $1/E_p$ or $1/\sqrt{E_p}$ scaling is shown in Fig. 21 normalized to the lowest-energy data point. Since the TNSA protons have time-of-flight spreading of order 50 ps, a rapidly-decaying electromagnetic field could explain the data, as the higher-energy protons would be deflected by a stronger path-integrated field than the lower-energy protons. However, the field would have to be present on both shots (with and without the heating target), which is unlikely.

A more likely possibility is that the protons creating the image in Fig. 20 are not born at the expected location (i.e. where the short-pulse laser hits the target foil). Evidence for multiple proton sources in these types of experiments has been observed in the TPIE data, illustrated by Fig. 22. Multiple sources of protons are also problematic for potential stopping-power experiments, as the path length traversed by protons in the subject plasma depends on where the protons are born.

Finally, another crosstalk concern is that the proton-heating

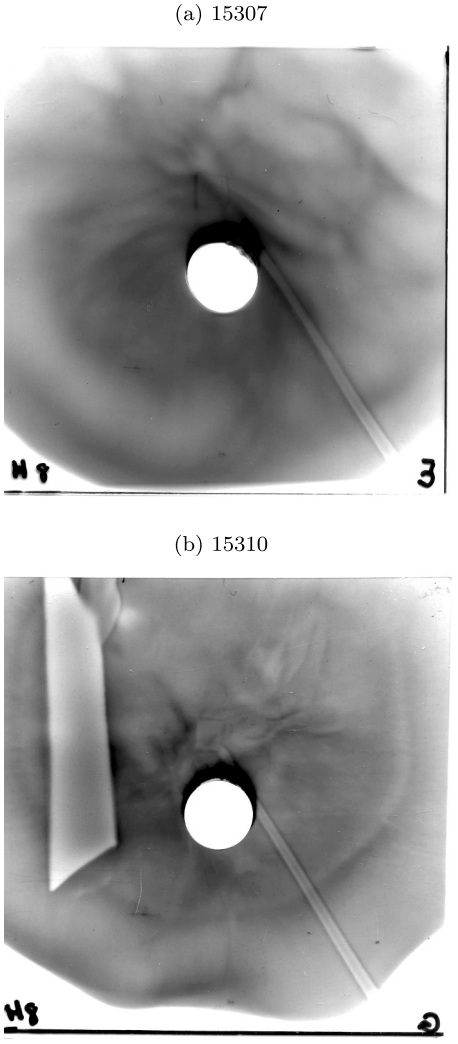

Fig. 20. RCF image of the probing protons (see Fig. 19) from two integrated shots: 15307 without proton heating (slab only), and 15310 with a heated slab. The film is 7cm square.

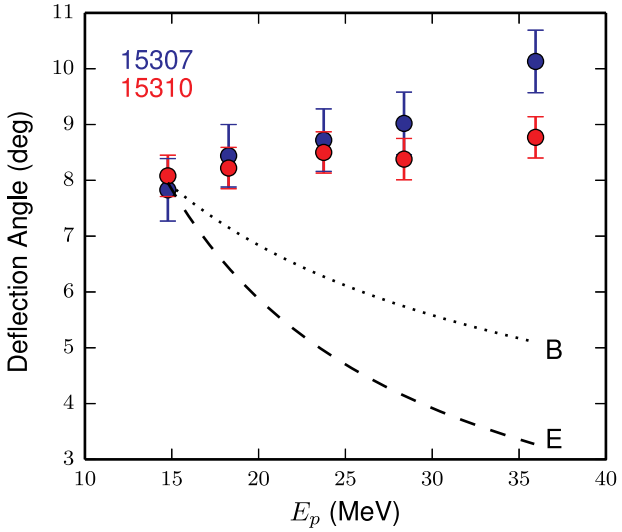

Fig. 21. Proton deflection angle versus energy inferred via slab image location. In comparison to the expected $1/E_p$ and $1/\sqrt{E_p}$ scaling for E and B field deflections, no change with energy is observed.

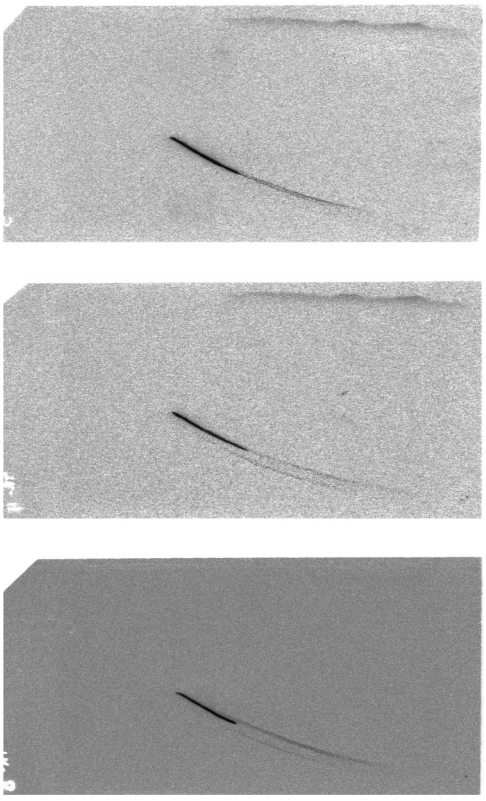

Fig. 22. Raw TPIE signals from proton source experiments, where multiple proton parabolas are clearly visible. The fiducial is at the lower right, and magnetic (electric) displacement is horizontal (vertical). From left to right, data are from shots 17414, 17416, and 17418. The TPIE CR-39 is 5 × 10 cm.

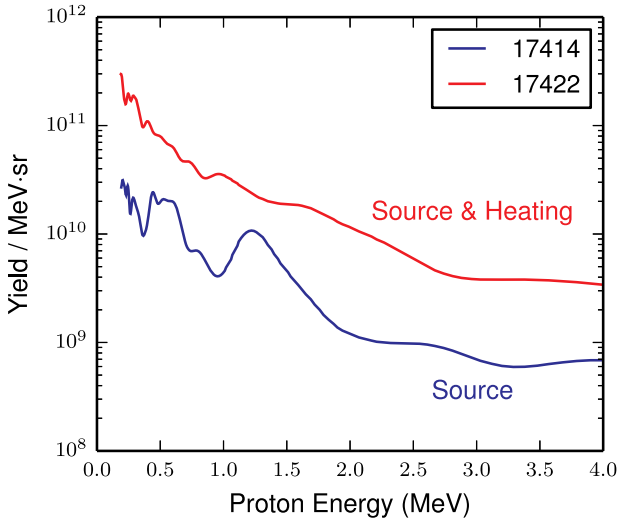

Fig. 23. Spectra from proton source only (17414) and proton source with a proton-heated slab (17422). The proton source was a CVD wafer with CH overcoating driven by 40 J/1 ps (~ 3 × 10^{18} W/cm^2) pulse. The proton heating drive was 150 J/10 ps (~ 1 × 10^{18} W/cm^2).

interaction may generate protons that would be detected on the spectrometer, even with the orthogonal line-of-sight (see Fig. 19). For example, this could happen if the slab charges to an electric potential of several MV. This was tested with two shots: 17414, with only the proton probing source, and shot 17422, using an identical proton source but with a proton-heated slab. These spectra are shown in Fig. 23 (shot 17414 also in Fig. 11). The shot with the proton heating displays considerably higher proton flux across the entire energy range. This data

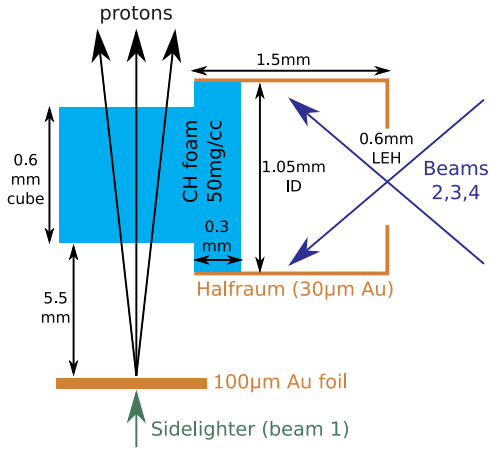

Fig. 24. Experimental geometry for the halfraum-heated foam experiment. A halfraum (right) drives a heat wave in a low-density foam, which is probed by TNSA-generated energetic protons.

suggests that ~ 5 × more protons from the heating than the probing are detected in the spectrometer, even though the spectrometer is orthogonal to the heating beam. This would represent a very small S/B for any potential stopping-power measurement, and it is not clear if this effect can be mitigated for a *dE/dx* experiment using a proton-isochorically heated subject target.

5.2. Hohlraum-heated subject plasma

Experiments were conducted at OMEGA EP to test the feasibility of using radiatively-heated foams as a subject target for stopping-power experiments. The experimental geometry is shown in Fig. 3. The concept is to use a halfraum (right) to launch a supersonic heat wave into a low-density foam (left, blue), which would be quasi-isochorically heated to warm (~ 10 s-100 eV) conditions.

The detailed target design is shown in Fig. 24. Three of the OMEGA EP beams (#2,3,4) were used in long-pulse mode to drive the hohlraum with a 2 ns long pulse shape and 2 kJ of energy per beam. The heat wave propagated through the low-density (50 mg/cm^3) CH foam. A 300μm thick region of the foam was inserted into the halfraum, providing a 'tamp' so that hydrodynamic motion is minimized in the sampling region. At the end of the halfraum, a 600μm cube of foam was the subject plasma for the experiment, presenting a uniform thickness of material along the proton propagation direction. The probing protons were generated with the sidelighter beam, using a 40 J/1 ps (~ 3 × 10^{18} W/cm^2) pulse incident upon a 100μm-thick Au foil.

A radiation temperature of up to 150 eV was expected based on scaling relations and prior work [49]. A HYADES simulation of the foam 2ns after the start of the drive, well after the heat wave has propagated through, is shown in Fig. 4.

This experiment was diagnosed with radiochromic film (RCF) and the Electron-Proton-Positron Spectrometer (EPPS) [50][3] The RCF was used to diagnose the spatial distribution of the proton beam. A selection of low-energy films is shown in Fig. 25.

In the proton images, the halfraum and foam outline are clearly apparent in the cold foam (undriven hohlraum) experiment, shot 18860 (upper left). When the hohlraum drive and heating starts 2 ns before the proton probing, shot 18861, significant distortion of the proton image is observed due to electromagnetic fields. The last two shots (18864 and 18866) probed the foam earlier (1 ns after the start of the heating), and show significantly less distortion. However, a filamentary field

[3] Unlike the prior shots, EPPS was used due to its higher solid angle relative to TPIE, which was expected to be improve the data quality with the thicker Au targets and lower laser energy.

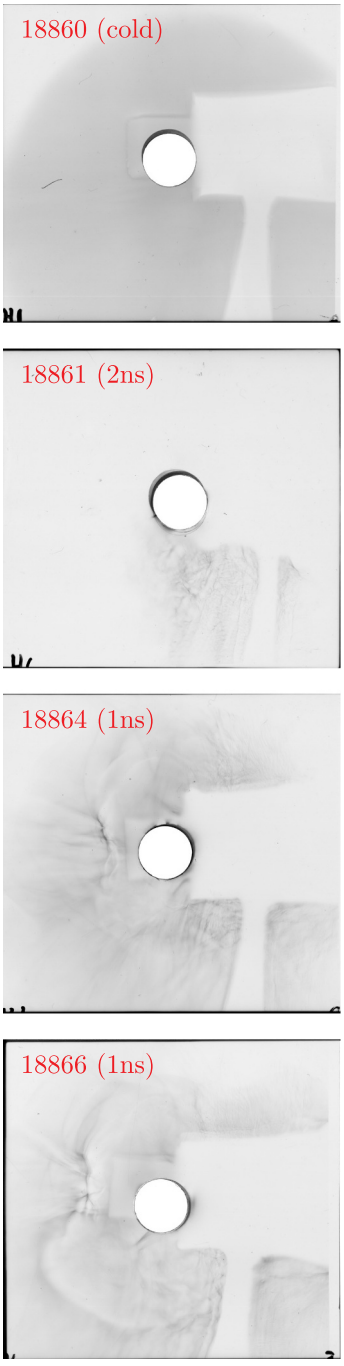

Fig. 25. 5 MeV proton images from RCF for four halfram shots. **18860:** Cold foam (undriven halfraum), **18861:** heated foam (2 ns after start of the hohlraum drive), **18864 & 18866:** heated foam (1 ns after start of the hohlraum drive).

structure around the subject target is still apparent. Unlike the proton isochoric heating experiment, no anomalous deflection of the entire proton beam is observed in this configuration.

EPPS was used to measure the proton spectrum transmitted through the foam (through the hole in the center of the RCF). The spectra are shown in Fig. 26. Shot 18857 (black curve) had the proton source only, shot 18860 (red) had an unheated foam, and the remaining shots all had heated foams. On shot 18861, the proton probing occurred 2ns after the start of the hohlraum heating, while the other three shots were probed 1 ns after the start of heating.

The proton spectrum in the 2 ns probing case is clearly suppressed

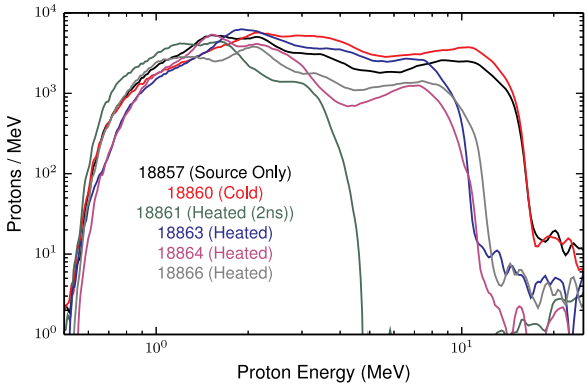

Fig. 26. EPPS proton spectra measured on all shots.

relative to the other shots, corroborating the RCF image (Fig. 25). Likely this is caused by suppression of the proton generation: the hohlraum may preheat the proton source foil. Oddly, the shot with a cold foam is seen to have a higher intensity and energy proton spectrum than the source-only shot, opposite to what we would expect. The three nominally-identical shots, 18863-6, also show significant variation. This suggests that the shot-to-shot repeatability of the TNSA proton source in this configuration is still not adequate for a stopping power measurement.

On a separate halfraum-only shot, the EPPS detector recorded no energetic proton signal, indicating that the halfraum scheme eliminates direct 'crosstalk', i.e. the hohlraum target does not generate protons (no background for the stopping measurement).

6. Conclusion

Platform test and development experiments have been conducted, where the goal was to study charged-particle stopping power using petawatt lasers, which would potentially have several potential advantages over long-pulse experiments [13]. Fundamentally, such an experiment requires well-understood heating of a subject target, and an independent source of well-characterized probing protons that would traverse the subject plasma.

The proton sources considered are planar foils driven by a short-pulse petawatt laser, generating energetic charged particles via the TNSA mechanism. In plain foils, smoother foil substrates (smoother Au, Si wafers, and CVD wafers) were used in an attempt to improve proton beam uniformity, for the first time on OMEGA EP. At high intensity, laser-seeded filamentation instabilities appear to dominate the beam transverse non-uniformities. These non-uniformities persist at lower intensity; a potential advantage to using CVD [45] is suggested by the data. Plastic-coated targets were tried in an attempt to replicate prior work [25]. Quasi-monoenergetic peaks in the proton spectrum are sometimes observed using this technique, but are not repeatable. The lack of repeatability may be related to the uniformity issues. A potential route to mitigating these issues is to use thicker targets or lower intensity drives.

Proton isochoric heating has been studied as a method of generating the subject plasma. TNSA-generated fast protons traverse a subject 'slab' target, depositing energy quasi-volumetrically. The slab expansion is studied using X-ray radiography, which shows significant longitudinal non-uniformities along the proton heating axis. Comparison to simulations suggest that the expansion is not governed by hydrodynamic rarefaction, but that an electrostatic 'Coulomb explosion' may be responsible for much of the slab motion. Significant electromagnetic fields are observed in self-radiographs around the isochorically-heated sample, which are highly sensitive to the experimental geometry. These fields are sufficiently strong that they raise questions about the efficacy of proton isochoric heating and are a concern for interpreting such

experiments. Furthermore, the proton heating targets appear to interfere with the probing proton propagation, and the proton heating generates signal in the proton spectrometer at much higher levels than the probe itself, even though the heating beam is orthogonal to the proton probing direction.

In the last set of shots, a halfraum-driven radiatively-heated foam configuration was explored. In this case, the cross-talk issues between the two targets appear less severe. However, the shot-to-shot repeatability in the proton source or proton probing is not adequate for a stopping power measurement.

This variety of effects presents a several challenges to realizing a stopping power experiment on OMEGA EP that would need to be mitigated. For the proton source, using a substantially thicker Au target and low intensity may generate a well-understood exponential spectrum, which could be used for the proton probing. The reproducibility requirement flows from expected differences in stopping-power theories (e.g. see Fig. 5), suggesting energy uniformities of 5–10% are required. Based on this data, proton isochoric heating does not seem to be a promising technique for this type of experiment unless substantial mitigation of the uniformity and charging issues can be developed. Using the long-pulse beams on OMEGA EP to generate a radiatively- or shock-heated subject plasma is a more promising technique based on our data, and if coupled with a reliable proton probing technique could be a compelling route towards a short-pulse laser stopping power measurement.

Declaration of Competing Interest

The authors declare that they have no known competing financial interests or personal relationships that could have appeared to influence the work reported in this paper.

Acknowledgments

We thank the operations personnel at OMEGA EP and the target fabrication group at General Atomics for supporting these experiments. This work was performed under the auspices of the U.S. Department of Energy by Lawrence Livermore National Laboratory in part under Contract DE-AC52-07NA27344 and supported by the U.S. DOE Early Career Research Program (Fusion Energy Sciences) under FWP SCW1658. This document was prepared as an account of work sponsored by an agency of the United States government. Neither the United States government nor Lawrence Livermore National Security, LLC, nor any of their employees makes any warranty, expressed or implied, or assumes any legal liability or responsibility for the accuracy, completeness, or usefulness of any information, apparatus, product, or process disclosed, or represents that its use would not infringe privately owned rights. Reference herein to any specific commercial product, process, or service by trade name, trademark, manufacturer, or otherwise does not necessarily constitute or imply its endorsement, recommendation, or favoring by the United States government or Lawrence Livermore National Security, LLC. The views and opinions of authors expressed herein do not necessarily state or reflect those of the United States government or Lawrence Livermore National Security, LLC, and shall not be used for advertising or product endorsement purposes.

References

[1] W.H. Bragg, R. Kleeman, Xxxix. on the α particles of radium, and their loss of range in passing through various atoms and molecules, Lond. Edinb. Dublin Philos. Mag. J. Sci. 10 (57) (1905) 318–340.

[2] N. Bohr, On the decrease of velocity of swiftly moving electrified particles in passing through matter, Philos. Mag. 30 (1915) 581–612, https://doi.org/10.1080/14786441008635432.

[3] H. Bethe, Zur Theorie des Durchgangs schneller Korpuskularstrahlen durch Materie, Ann. Phys. 5 (1930) 325–400.

[4] F. Bloch, Zur Bremsung rash bewegter Teilchen beim Durchgang durch Materie, Ann. Phys. 16 (1933) 285–320.

[5] J. Ziegler, J. Biersack, U. Littmark, The stopping and range of ions in matter, Pergamon, New York, 1985.

[6] J. Nuckolls, L. Wood, A. Thiessen, G. Zimmerman, Laser compression of matter to super-high densities: thermonuclear (CTR) applications, Nature 239 (1972) 139–142, https://doi.org/10.1038/239139a0.

[7] J. Lindl, Development of the indirect-drive approach to inertial confinement fusion and the target physics basis for ignition and gain, Phys. Plasmas 2 (1995) 3933–4024, https://doi.org/10.1063/1.871025.

[8] O.A. Hurricane, P.T. Springer, P.K. Patel, D.A. Callahan, K. Baker, D.T. Casey, L. Divol, T. Dppner, D.E. Hinkel, M. Hohenberger, L.F. Berzak Hopkins, C. Jarrott, A. Kritcher, S. Le Pape, S. Maclaren, L. Masse, A. Pak, J. Ralph, C. Thomas, P. Volegov, A. Zylstra, Approaching a burning plasma on the NIF, Phys. Plasmas 26 (5) (2019) 052704, https://doi.org/10.1063/1.5087256.

[9] A.B. Zylstra, O.A. Hurricane, On alpha-particle transport in inertial fusion, Phys. Plasmas 26 (2019) 062701.

[10] M. Roth, T.E. Cowan, M.H. Key, S.P. Hatchett, C. Brown, W. Fountain, J. Johnson, D.M. Pennington, R.A. Snavely, S.C. Wilks, K. Yasuike, H. Ruhl, F. Pegoraro, S.V. Bulanov, E.M. Campbell, M.D. Perry, H. Powell, Fast ignition by intense laser-accelerated proton beams, Phys. Rev. Lett. 86 (2001) 436–439, https://doi.org/10.1103/PhysRevLett.86.436.

[11] M. Tabak, D. Callahan-Miller, Design of a distributed radiator target for inertial fusion driven from two sides with heavy ion beams, Phys. Plasmas 5 (5) (1998) 1895–1900, https://doi.org/10.1063/1.872860.

[12] T. Boehly, D. Brown, R. Craxton, et al., Initial performance results of the OMEGA laser system, Opt. Commun. 133 (1–6) (1997) 495–506, https://doi.org/10.1016/S0030-4018(96)00325-2.

[13] A.B. Zylstra, J.A. Frenje, P.E. Grabowski, C.K. Li, G.W. Collins, P. Fitzsimmons, S. Glenzer, F. Graziani, S.B. Hansen, S.X. Hu, M.G. Johnson, P. Keiter, H. Reynolds, J.R. Rygg, F.H. Séguin, R.D. Petrasso, Measurement of charged-particle stopping in warm dense plasma, Phys. Rev. Lett. 114 (2015) 215002, https://doi.org/10.1103/PhysRevLett.114.215002.

[14] A.B. Zylstra, J.A. Frenje, P.E. Grabowski, C.K. Li, G.W. Collins, P. Fitzsimmons, S. Glenzer, F. Graziani, S.B. Hansen, S.X. Hu, M.G. Johnson, P. Keiter, H. Reynolds, J.R. Rygg, F.H. Séguin, R.D. Petrasso, J. Phys. 717 (2016) 012118.

[15] J.A. Frenje, P.E. Grabowski, C.K. Li, F.H. Séguin, A.B. Zylstra, M. Gatu Johnson, R.D. Petrasso, V.Y. Glebov, T.C. Sangster, Measurements of ion stopping around the Bragg peak in high-energy-density plasmas, Phys. Rev. Lett. 115 (2015) 205001, https://doi.org/10.1103/PhysRevLett.115.205001.

[16] J.A. Frenje, R. Florido, R. Mancini, T. Nagayama, P.E. Grabowski, H. Rinderknecht, H. Sio, A. Zylstra, M. Gatu Johnson, C.K. Li, F.H. Séguin, R.D. Petrasso, V.Y. Glebov, S.P. Regan, Experimental validation of low-z ion-stopping formalisms around the Bragg peak in high-energy-density plasmas, Phys. Rev. Lett. 122 (2019) 015002, https://doi.org/10.1103/PhysRevLett.122.015002.

[17] W. Cayzac, A. Frank, A. Ortner, V. Bagnoud, M. Basko, S. Bedacht, C. Bläser, A. Blažević, S. Busold, O. Deppert, et al., Experimental discrimination of ion stopping models near the Bragg peak in highly ionized matter, Nat. Commun. 8 (2017) 15693.

[18] D. Strickland, G. Mourou, Compression of amplified chirped optical pulses, Opt. Commun. 55 (6) (1985) 447–449.

[19] F.R. Graziani, V.S. Batista, L.X. Benedict, J.I. Castor, H. Chen, S.N. Chen, C.A. Fichtl, J.N. Glosli, P.E. Grabowski, A.T. Graf, S.P. Hau-Riege, A.U. Hazi, S.A. Khairallah, L. Krauss, A.B. Langdon, R.A. London, A. Markmann, M.S. Murillo, D.F. Richards, H.A. Scott, R. Shepherd, L.G. Stanton, F.H. Streitz, M.P. Surh, J.C. Weisheit, H.D. Whitley, Large-scale molecular dynamics simulations of dense plasmas: the cimarron project, High Energy Density Phys. 8 (1) (2012) 105–131, https://doi.org/10.1016/j.hedp.2011.06.010.

[20] L. Waxer, D. Maywar, J. Kelly, T. Kessler, B. Kruschwitz, S. Loucks, R. McCrory, D. Meyerhofer, S. Morse, C. Stoeckl, J. Zuegel, High-energy petawatt capability for the Omega laser, Opt. Photonics News 16 (7) (2005) 30–36.

[21] S. Hatchett, C. Brown, T. Cowan, E. Henry, J. Johnson, M. Key, J. Koch, A. Langdon, B. Lasinski, R. Lee, A. Mackinnon, D. Pennington, M. Perry, T. Phillips, M. Roth, T. Sangster, M. Singh, R. Snavely, M. Stoyer, S. Wilks, K. Yasuike, Electron, photon, and ion beams from the relativistic interaction of Petawatt laser pulses with solid targets, Phys. Plasmas 7 (2000), https://doi.org/10.1063/1.874030.

[22] A.J. Mackinnon, P.K. Patel, M. Borghesi, R.C. Clarke, R.R. Freeman, H. Habara, S.P. Hatchett, D. Hey, D.G. Hicks, S. Kar, M.H. Key, J.A. King, K. Lancaster, D. Neely, A. Nikkro, P.A. Norreys, M.M. Notley, T.W. Phillips, L. Romagnani, R.A. Snavely, R.B. Stephens, R.P.J. Town, Proton radiography of a laser-driven implosion, Phys. Rev. Lett. 97 (4) (2006), https://doi.org/10.1103/PhysRevLett.97.045001.

[23] A.B. Zylstra, C.K. Li, H.G. Rinderknecht, F.H. Séguin, R.D. Petrasso, C. Stoeckl, D.D. Meyerhofer, P. Nilson, T.C. Sangster, S. Le Pape, A. Mackinnon, P. Patel, Using high-intensity laser-generated energetic protons to radiograph directly driven implosions, Rev. Sci. Instrum. 83 (1) (2012), https://doi.org/10.1063/1.3680110.

[24] P.K. Patel, A.J. Mackinnon, M.H. Key, T.E. Cowan, M.E. Foord, M. Allen, D.F. Price, H. Ruhl, P.T. Springer, R. Stephens, Isochoric heating of solid-density matter with an ultrafast proton beam, Phys. Rev. Lett. 91 (2003) 125004, https://doi.org/10.1103/PhysRevLett.91.125004.

[25] H. Schwoerer, S. Pfotenhauer, O. Jäckel, K.-U. Amthor, B. Liesfeld, W. Ziegler, R. Sauerbrey, K. Ledingham, T. Esirkepov, Laser-plasma acceleration of quasi-monoenergetic protons from microstructured targets, Nature 439 (2006) 445–448, https://doi.org/10.1038/nature04492.

[26] S.N. Chen, S. Atzeni, T. Gangolf, M. Gauthier, D.P. Higginson, R. Hua, J. Kim, F. Mangia, C. McGuffey, J.R. Marquès, R. Riquier, H. Pépin, R. Shepherd, O. Willi,

F.N. Beg, C. Deutsch, J. Fuchs, Experimental evidence for the enhanced and reduced stopping regimes for protons propagating through hot plasmas, Sci. Rep. 8 (1) (2018) 14586, https://doi.org/10.1038/s41598-018-32726-2.
[27] D. Jahn, D. Schumacher, C. Brabetz, F. Kroll, F.E. Brack, J. Ding, R. Leonhardt, I. Semmler, A. Blažević, U. Schramm, M. Roth, Focusing of multi-mev, sub-nanosecond proton bunches from a laser-driven source, Phys. Rev. Accel. Beams 22 (2019) 011301, https://doi.org/10.1103/PhysRevAccelBeams.22.011301.
[28] A. Tauschwitz, M. Basko, A. Frank, V. Novikov, A. Grushin, A. Blazevic, M. Roth, J. Maruhn, 2D radiation-hydrodynamics modeling of laser-plasma targets for ion stopping measurements, High Energy Density Phys. 9 (1) (2013) 158–166, https://doi.org/10.1016/j.hedp.2012.12.004.
[29] S. Faik, A. Tauschwitz, M.M. Basko, J.A. Maruhn, O. Rosmej, T. Rienecker, V.G. Novikov, A.S. Grushin, Creation of a homogeneous plasma column by means of hohlraum radiation for ion-stopping measurements, High Energy Density Phys. 10 (2014) 47–55, https://doi.org/10.1016/j.hedp.2013.10.002.
[30] A. Ortner, S. Faik, D. Schumacher, M. Basko, A. Blazevic, S. Busold, S. Bedacht, W. Cayzac, A. Frank, D. Kraus, T. Rienecker, G. Schaumann, A. Tauschwitz, F. Wagner, M. Roth, A novel double hohlraum target to create a moderately coupled plasma for ion stopping experiments, Nucl. Instrum. Methods Phys. Res. Sect. B 343 (2015) 123–131, https://doi.org/10.1016/j.nimb.2014.11.047.
[31] O.N. Rosmej, N. Suslov, D. Martsovenko, G. Vergunova, N. Borisenko, N. Orlov, T. Rienecker, D. Klir, K. Rezack, A. Orekhov, L. Borisenko, E. Krousky, M. Pfeifer, R. Dudzak, R. Maeder, M. Schaechinger, A. Schoenlein, S. Zaehter, J. Jacoby, J. Limpouch, J. Ullschmied, N. Zhidkov, The hydrodynamic and radiative properties of low-density foams heated by X-rays, Plasma Phys. Controlled Fusion 57 (9) (2015) 94001, https://doi.org/10.1088/0741-3335/57/9/094001.
[32] J.T. Larsen, S.M. Lane, HYADES-A plasma hydrodynamics code for dense plasma studies, Journal of Quantitative Spectroscopy and Radiative Transfer 51 (1-2) (1994) 179–186, https://doi.org/10.1016/0022-4073(94)90078-7. Special Issue Radiative Properties of Hot Dense Matter
[33] C. Li, R. Petrasso, Charged-particle stopping powers in inertial confinement fusion plasmas, Phys. Rev. Lett. 70 (20) (1993) 3059, https://doi.org/10.1103/PhysRevLett.70.3059.
[34] C. Li, R. Petrasso, Erratum: charged-particle stopping powers in inertial confinement fusion plasmas, Phys. Rev. Lett. (2015).
[35] A. Zylstra, et al., Modified parameterization of the Li-Petrasso Charged-Particle Stopping Power Theory, submitted to Phys. Plasmas (2019).
[36] L.S. Brown, D.L. Preston, R.L. Singleton Jr., Charged particle motion in a highly ionized plasma, Phys. Rep. 410 (4) (2005) 237–333, https://doi.org/10.1016/j.physrep.2005.01.001.
[37] G. Maynard, C. Deutsch, Energy loss and straggling of ions with any velocity in dense plasmas at any temperature, Phys. Rev. A 26 (1982) 665, https://doi.org/10.1103/PhysRevA.26.665.
[38] G. Maynard, C. Deutsch, Born random phase approximation for ion stopping in an arbitrary degenerate electron fluid, J. Phys. 46 (1985) 1113–1122, https://doi.org/10.1051/jphys:019850046070111300.
[39] D. Hey, M. Key, A. Mackinnon, A. MacPhee, P. Patel, R. Freeman, L. Van Woerkom, C. Castaneda, Use of GafChromic film to diagnose laser generated proton beams, Rev. Sci. Instrum. 79 (2008), https://doi.org/10.1063/1.2901603.
[40] N. Sinenian, Fast-Ion Spectrometry of ICF Implosions and Laser-Foil Experiments at the Omega and MTW Laser Facilities, Massachusetts Institute of Technology, 2013 Ph.D. thesis.
[41] J.A. Cobble, K.A. Flippo, D.T. Offermann, F.E. Lopez, J.A. Oertel, D. Mastrosimone, S.A. Letzring, N. Sinenian, High-resolution Thomson parabola for ion analysis, Rev. Sci. Instrum. 82 (11) (2011), https://doi.org/10.1063/1.3658048.
[42] C.G. Freeman, G. Fiksel, C. Stoeckl, N. Sinenian, M.J. Canfield, G.B. Graeper, A.T. Lombardo, C.R. Stillman, S.J. Padalino, C. Mileham, T.C. Sangster, J.A. Frenje, Calibration of a Thomson parabola ion spectrometer and Fujifilm imaging plate detectors for protons, deuterons, and alpha particles, Rev. Sci. Instrum. 82 (7) (2011), https://doi.org/10.1063/1.3606446.
[43] A. Zylstra, Using fusion-product spectroscopy to study inertial fusion implosions, stopping power, and astrophysical nucleosynthesis at OMEGA and the NIF, Massachusetts Institute of Technology, 2015 Ph.D. thesis.
[44] A. Hazi, R. Shepherd, 2012, (private communication).
[45] P. McKenna, A.P.L. Robinson, D. Neely, M.P. Desjarlais, D.C. Carroll, M.N. Quinn, X.H. Yuan, C.M. Brenner, M. Burza, M. Coury, P. Gallegos, R.J. Gray, K.L. Lancaster, Y.T. Li, X.X. Lin, O. Tresca, C.-G. Wahlström, Effect of lattice structure on energetic electron transport in solids irradiated by ultraintense laser pulses, Phys. Rev. Lett. 106 (2011), https://doi.org/10.1103/PhysRevLett.106.185004.
[46] D.A. MacLellan, D.C. Carroll, R.J. Gray, N. Booth, M. Burza, M.P. Desjarlais, F. Du, B. Gonzalez-Izquierdo, D. Neely, H.W. Powell, A.P.L. Robinson, D.R. Rusby, G.G. Scott, X.H. Yuan, C.-G. Wahlström, P. McKenna, Annular fast electron transport in silicon arising from low-temperature resistivity, Phys. Rev. Lett. 111 (2013), https://doi.org/10.1103/PhysRevLett.111.095001.
[47] M.J.-E. Manuel, N. Sinenian, F.H. Séguin, C.K. Li, J.A. Frenje, H.G. Rinderknecht, D.T. Casey, A.B. Zylstra, R.D. Petrasso, F.N. Beg, Mapping return currents in laser-generated Z-pinch plasmas using proton deflectometry, Appl. Phys. Lett. 100 (20) (2012), https://doi.org/10.1063/1.4718425.
[48] N. Sinenian, M.J.-E. Manuel, J.A. Frenje, F.H. Séguin, C.K. Li, R.D. Petrasso, An empirical target discharging model relevant to hot-electron preheat in direct-drive implosions on OMEGA, Plasma Phys. Controlled Fusion 55 (4) (2013), https://doi.org/10.1088/0741-3335/55/4/045001.
[49] D. Hinkel, Private Communication (2014).
[50] H. Chen, A.J. Link, R. van Maren, P.K. Patel, R. Shepherd, S.C. Wilks, P. Beiersdorfer, High performance compact magnetic spectrometers for energetic ion and electron measurement in ultraintense short pulse laser solid interactionsa), Rev. Sci. Instrum. 79 (10) (2008), https://doi.org/10.1063/1.2953679.